Study of broadband THz time-domain spectroscopy at different relative humidity levels

Chiajen Lin (林家任), Ichen Ho (何宜貞), and X. C. Zhang (张希成)[*]

Center for Terahertz Research, Rensselaer Polytechnic Institute, Troy, NY 12180-3590, USA

[*]*Corresponding author: Zhangxc@rpi.edu*

Received September 13, 2011; accepted October 8, 2011; posted online December 8, 2011

Two detection techniques of broadband terahertz (THz) time-domain spectroscopy-THz air-biased coherent detection (THz-ABCD; from 0.3 to 14 THz) and electro-optical (EO) detection (from 0.3 to 7 THz) – are both performed at several different relative humidity levels. The THz power exponentially decays with the increase in relative humidity. The dynamic range of the main pulse in the time domain linearly decreases as the relative humidity increases from 0% to 40%, and linear fittings show that the slopes are –0.017 and –0.019 for THz-ABCD and EO detection, respectively. Because of the multiple reflections caused by the crystal in the common EO detection, THz-ABCD has better spectral resolution (17 GHz) than that of EO detection (170 GHz). The spectrum of water vapor absorption measured by THz-ABCD is also compared with that measured by the Fourier transform infrared spectroscopy (FTIR).

　　OCIS codes: 300.6495, 320.7150, 300.6500.
　　doi: 10.3788/COL201210.043001.

Terahertz (THz) waves have brought benefits to a variety of applications, including biomedical investigation, non-destructive inspection, and material characterization[1−3]. This is because most rotational and vibrational resonances of molecules and chemical compounds are located in such frequency range. However, water vapor attenuates THz waves when it propagates in the atmosphere. Grischkowsky *et al.* have reported a number of research about water vapor absorption in the THz range, especially from 0.2 to 2 THz[4,5].

On the other hand, the astronomical observations at THz frequencies are significantly impacted by daily weather, varying seasons, as well as different altitudes and geographical locations. To reduce the attenuation by water vapor over an absorbing propagation path, many groups have driven submillimeter-wave telescopes to the highest, driest, and coldest sites for ground-based astronomical telescopes operating at THz frequencies[6,7]. THz time-domain spectroscopy (THz-TDS) using selected gases as an emitter and sensor now provides an intense THz field, a broadband spectrum, and sensitive detection capabilities for studying material properties[8,9]. In terms of remote sensing, a promising technique is the use of gases as the emitter and the sensor[10,11]. To investigate the performance of broadband THz-TDS in various environments, this study uses nitrogen gas as THz emitter along with two broadband detection techniques – THz air-biased coherent detection (THz-ABCD) and electro-optical (EO) sampling with a GaP crystal[12,13] – to measure the absorption spectra of water vapor at different relative humidity (RH) levels.

The broadband THz spectrometer with THz-ABCD and EO sampling with a GaP crystal is schematically shown in Fig. 1. A Ti-sapphire amplified laser (Coherent Libra) with a central wavelength of 800 nm, 50-fs pulse duration, 1.3-mJ pulse energy, and 3-kHz repetition rate is used as the optical source. The laser beam is split into two by an optical beam splitter. One beam has 85% of the energy passed through a 100-μm-thick type I beta barium borate (BBO) crystal, by which the

400-nm second harmonic (SH) beam is generated. The fundamental (ω) and SH (2ω) beams are focused with a lens of 150-mm effective focal length. The dominantly p-polarized THz emission from the laser-induced plasma is collimated and refocused by a pair of parabolic mirrors P1 (6" focal length) and P2 (4" focal length), respectively. A high-resistivity silicon wafer is used to block the residual fundamental and SH beams. The THz beam is then collimated and refocused by parabolic mirrors P3 (4" focal length) and P4 (2" focal length), respectively, at the detector. The propagation path length of the THz beam is 70 cm. The residual 15% of the optical energy is guided to a motorized delay stage and through the hole of the parabolic mirror P4 as the probe beam.

For THz-ABCD, both the THz and the optical probe beams are focused between two needle-shaped electrodes that are 1-mm apart. SH generation is induced through
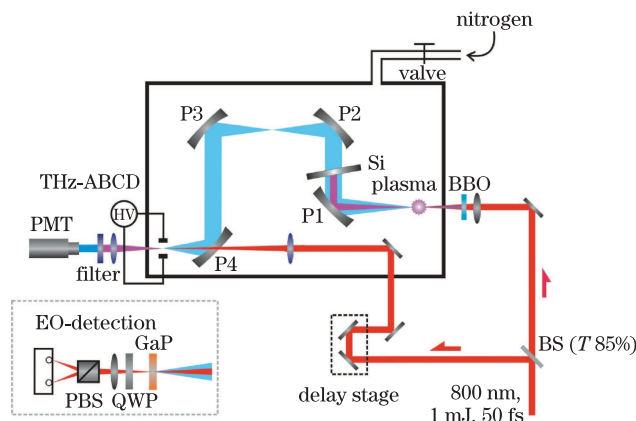

Fig. 1. Experimental setup. A Ti:sapphire amplified laser with 800 nm, 1.3-mJ pulse energy, and 50-fs pulse duration is used as the optical source, and the THz beam is generated by mixing 800-nm and 400-nm waves in the air plasma. The THz spectrum is detected with THz-ABCD and EO detection. BS: beam splitter; PBS: polarizing beam splitter; QWP: quarter-wave plate; PMT: photomultiplier tube.

the nonlinear interaction of the probe field, THz field, and local bias electric field, and its intensity is proportional to the THz electrical field and the local bias field strength. A laser-synchronized alternating bias of ±20 kV/cm at 500 Hz is applied by a high-voltage (HV) modulator. It introduces an AC external bias to the optical focus point between the two needle-shaped electrodes, where a bias-field-induced SH pulse is generated. The local bias provides heterodyne detection to improve the dynamic range (DR) and ensure coherent detection. The coherent field-induced SH generation is selected by several band pass filters and detected by a photomultiplier tube (PMT) (H7732-10, Hamamatsu, Japan). The THz electric field at the focus point is about 100 kV/cm.

The detector can be easily changed to EO sampling with a GaP crystal. For EO sampling, the pump beam is chopped by a mechanical chopper to modulate the THz wave. Both the THz and the optical probe beams are focused on a <110>-cut, 0.22-mm-thick GaP crystal. A pair of identical photodiodes is used to effectively cancel laser noise.

The setup is placed in a box, and the RH inside the enclosure is controlled by purging dry nitrogen. A commercial hygrometer (Sper Scientific 800014, Micro Precision Calibration, USA) is used to monitor the RH value. The accuracy of RH is controlled at ±1%. The water vapor absorption spectra are measured at room temperature of 24 ± 0.2 °C during the experiment.

The time-domain waveforms at different RH are measured by THz-ABCD, as shown in Fig. 2. The main pulse is set to 0 ps. When RH increases, the pulse peak decreases, and the waveform starts to oscillate due to the absorption of water vapor. The insets of Fig. 2 show the magnified time-domain waveforms for RH = 50% and 70%. The single-cycle waveform becomes a multi-cycle waveform in the main pulse when RH rises above 50% and the DR[14] becomes difficult to determine.

The THz power is determined by integrating the signal power in the time domain. Figures 3(a) and (b) show the THz power as functions of RH measured with THz-ABCD and EO detection, respectively. The THz power exponentially decreases as RH increases for THz-ABCD and EO detection, which corresponds to the
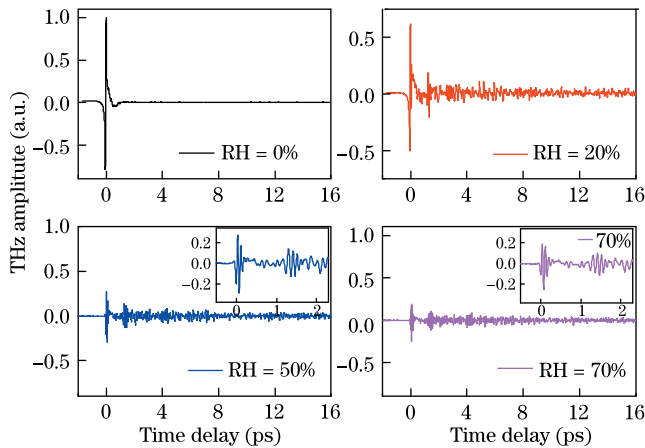
Fig. 2. Time-domain waveforms at different RHs measured by THz-ABCD. The insets are the magnified time-domain waveforms for RH = 50% and 70%; the main pulse starts to oscillate as RH is higher than 50%.
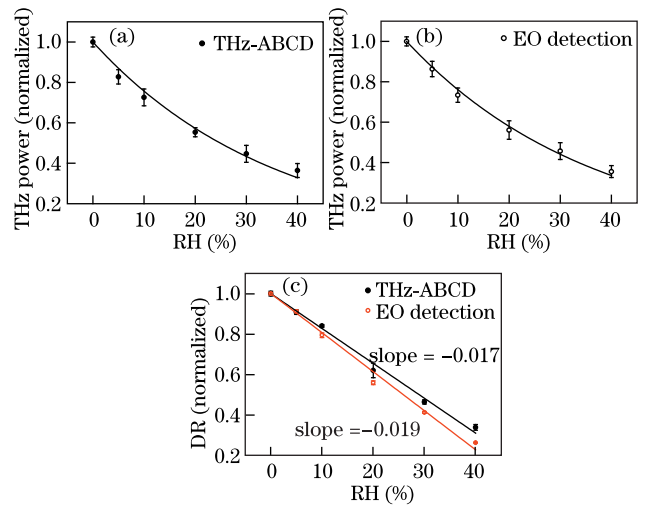
Fig. 3. Performances as functions of RH for THz-ABCD and EO detection. (a) THz power for THz-ABCD; (b) THz power for EO detection; (c) DR.
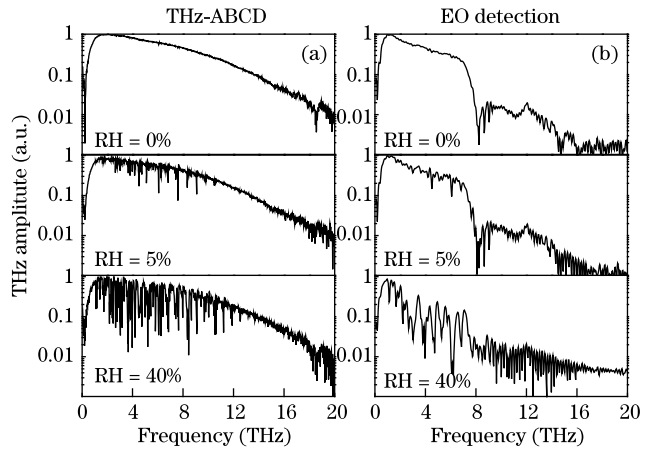
Fig. 4. Spectra under different RH conditions. (a) THz-ABCD and (b) EO detection. The upper figures, RH = 0%, indicate the reliable bandwidth (10% or higher amplitude with respect to the maximum), which is from 0.3 to 14 THz for THz-ABCD and from 0.3 to 7 THz for EO detection. The middle and lower figures show the spectra of water vapor absorption at RH = 5% and RH = 40%, respectively. In terms of the multiple reflections from the GaP crystal, THz-ABCD can provide a better spectral resolution than EO detection.

Beer-Lambert Law[15]. The Beer-Lambert Law indicates that the transmission power will exponentially decay with the increase in the density of absorbing particles. The results fit well with exponential decays. To make a clear comparison of the performances under different humidity levels, we normalized the DR by the maximum value corresponding to RH = 0%. Figure 3(c) shows the normalized DR of the time-domain waveforms as a function of RH. The DR decreases linearly as RH increases. The dots and circles are experimental data for THz-ABCD and EO detection, respectively, and the solid lines are the fitting results. The slopes are −0.017 and −0.019 for THz-ABCD and EO detection, respectively. The correlation coefficients for the fitting lines are about 0.99. The DR of EO detection decreases faster than that of THz-ABCD because the sensing bandwidth of the former mostly includes the frequencies of water

vapor absorption lines.

With fast Fourier transform, the spectra corresponding to THz-ABCD and EO detection at different RH conditions are shown in Figs. 4(a) and (b), respectively. The upper figures, RH = 0%, indicate the reliable bandwidth (10% or higher amplitude with respect to the maximum), which is from 0.3 to 14 THz for THz-ABCD and from 0.3 to 7 THz for EO detection. According to our experimental result, even though RH is about 5%, the water vapor absorption lines can be observed with both detection techniques. The spectra are shown in the middle of Fig. 4. However, for THz-ABCD, the absorption spectrum is not very clear at the lower frequency range, such as lower than 2 THz. For EO detection with the GaP crystal, the water vapor spectrum can also be observed, but not distinctly, due to the relative low RH = 5%. The lower figures, RH = 40%, show a clearer water vapor absorption spectra.

Considering the multiple reflections in crystals, the scan length is limited by the first reflection of waveform. For THz-ABCD, the first reflection of waveform appears at 60 ps after the main pulse, and the reflection is caused by a 3-mm-thick Si wafer used to block the residual fundamental and SH beams in the system. For EO detection, the first reflection due to the 0.22-mm-thick GaP crystal appears at 6 ps after the main pulse. Accordingly, the resolutions for THz-ABCD and EO detection is 17 GHz and 170 GHz, respectively, without using the zero-padding technique.

In the THz-ABCD measurement shown in Fig. 4(a), the water vapor absorption is primarily from 0.3 to 12 THz. At high frequencies of above 12 THz, THz-ABCD still has good performance even if the humidity is relatively high, indicating that there is less water vapor absorption at over 12 THz. On the other hand, the sensing bandwidth of EO detection includes most of the frequencies of water vapor absorption lines from 1 to 7 THz. This also explains why DR decreases faster in EO detection compared with THz-ABCD in Fig. 3(c).

To further verify the accuracy of the THz-ABCD system, we compare the result of water vapor measurement with that of the FTIR (Bruker IFS 66v/S), as shown in Fig. 5. The absorbance is defined as $-\log(I_{ref}/I_s)$, where I_{ref} is the intensity of the reference corresponding to RH = 0% and I_s is the intensity of the signal at different humidity levels. The magnification shows the spectra ranging from around 3 to 3.5 THz. The resolution of the FTIR is 1 GHz. We indicate the positions of the absorption lines to make a clear comparison; the discrepancy of the line positions is less than 0.005 THz. The results from the THz-ABCD and FTIR measurements are in good agreement. The variances of the line strengths measured with the two systems are mainly caused by the different path lengths of the THz beams as well as the different sensitivity levels of the two spectrometers. The beam path of the FTIR is 25 cm, which is less than that of THz-ABCD. Therefore, for many absorption lines, the absorbance measured by THz-ABCD is larger than that by FTIR, which can be observed at 3.048, 3.170, 3.215, 3.232, 3.335, 3.500, and 3.542 THz. For stronger absorption lines, such as at 2.977, 3.020, and 3.138 THz, the signals are relatively weak, and the different sensitivity levels between the two systems also cause the
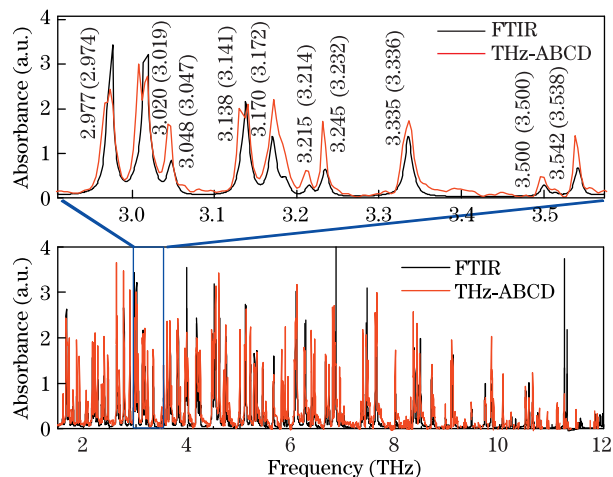

Fig. 5. Comparison of the water vapor absorption spectra between the THz-ABCD and the FTIR spectroscopy. The magnification shows the spectra ranging from around 3 to 3.5 THz, and the absorption lines are also shown. The numbers indicated in brackets are the positions for the FTIR and THz-ABCD, respectively. The results from THz-ABCD and FTIR measurements are in good agreement.

discrepancy. The frequency of each absorption line can be identified with high accuracy, and these absorptions also correspond to previous reports[16,17].

In conclusion, we demonstrate the performance of two detection methods of broadband THz-TDS – THz-ABCD and EO detection – at different relative humidity levels. The THz power exponentially decays as RH increases, as measured with THz-ABCD and EO detection. This result corresponds to the Beer-Lambert Law. The DR linearly decreases as RH increases from 0% to 40%, and the linear fittings show that the slopes are –0.017 and –0.019 for THz-ABCD and EO detection, respectively. The DR decreases faster in EO detection because its sensing bandwidth includes most of the frequencies of the water vapor absorption lines. Moreover, without zero-padding technique, the THz-ABCD has better spectral resolution than EO detection. Finally, a comparison of the water vapor absorption spectra between the THz-ABCD and the FTIR spectroscopy is performed, yielding results that are in good agreement.

References

1. B. Ferguson and X. Zhang, Nature Mater. **1,** 26 (2002).
2. P. H. Siegel, IEEE Trans. Microw. Theory Tech. **50,** 910 (2002).
3. M. Tonouchi, Nature Photon. **1,** 97 (2007).
4. M. van Exter, Ch. Fattinger, and D. Grischkowsky, Opt. Lett. **14,** 1128 (1989).
5. Y. Yang, A. Shutler, and D. Grischkowsky, Opt. Express **19,** 8830 (2011).

6. W. S. Holland, J. S. Greaves, B. Zuckerman, R. A. Webb, C. McCarthy, I. M. Coulson, D. M. Walther, W. R. F. Dent, W. K. Gear, and I. Robson, Nature **392,** 788 (1998).

7. H. Yang, C. A. Kulesa, C. K. Walker, N. F. H. Tothill, J. Yang, M. C. B. Ashley, X. Cui, L. Feng, J. S. Lawrence, D. M. Luong-Van, M. J. McCaughrean, J. W. V. Storey, L. Wang, X. Zhou, and Z. Zhu, Antarctica Publ. Astron. Soc. Pac. **122,** 190 (2010).

8. I-Chen Ho, X. Guo, and X.-C. Zhang, Opt. Express **18,** 2872 (2010).

9. I-Chen Ho and X.-C. Zhang, Appl. Phys. Lett. **98,** 241908 (2011).

10. J. Liu, J. Dai, S. L. Chin, and X.-C. Zhang, Nat. Photonics **4,** 627 (2010).

11. B. Clough, J. Liu, and X.-C Zhang, Opt. Lett. **35,** 3544 (2010).

12. X. Lu, N. Karpowicz, and X.-C. Zhang, J. Opt. Soc. Am. B **26,** A66 (2009).

13. Q. Wu and X.-C. Zhang, Appl. Phys. Lett. **70,** 1784 (1997).

14. M. Naftaly and R. Dudley, Opt. Lett. **34,** 1213 (2009).

15. H. Mitschele, Chem. Educ. Today **73,** A211 (1996).

16. G. Klatt, R. Gebs, H. Schäfer, M. Nagel, C. Janke, A. Bartels, and T. Dekorsy, IEEE J. Sel. Top. Quant. **17,** 159 (2011).

17. L. S. Rothman, I. Gordon, A. Barbe, D. Benner, P. Bernath, M. Birk, V. Boudon, L. Brown, A. Campargue, J.-P. Champion, K. Chance, L. Coudert, V. Dana, V. Devi, S. Fally, J.-M. Flaud, R. Gamache, A. Goldman, D. Jacquemart, I. Kleiner, N. Lacome, W. Lafferty, J.-Y. Mandin, S. Massie, S. Mikhailenko, C. Miller, N. Moazzen-Ahmadi, O. Naumenko, A. Nikitin, J. Orphal, V. Perevalov, A. Perrin, A. Predoi-Cross, C. Rinsland, M. Rotger, M. Simeckov'a, M. Smith, K. Sung, S. Tashkun, J. Tennyson, R. Toth, A. Vandaele, and J. V. Auwera, J. Quant. Spectrosc. Radiat. Transfer **110,** 533 (2009).